WILEY

The dynamics of a healthy and infected red blood cell in flow through constricted channels: A DPD simulation

Sazid Zamal Hoque[1] | D. Vijay Anand[2] | B. S. V. Patnaik[1] (ORCID)

[1] Department of Applied Mechanics, Indian Institute of Technology Madras, Chennai 600036, India

[2] Department of Mechanical Engineering, Indian Institute of Science, Bangalore 560012, India

Correspondence
B. S. V. Patnaik, Department of Applied Mechanics, Indian Institute of Technology Madras, Chennai 600036, India.
Email: bsvp@iitm.ac.in

Abstract

Understanding the dynamics of red blood cell (RBC) motion under in silico conditions is central to the development of cost-effective diagnostic tools. Specifically, unraveling the relationship between the rheological properties and the nature of shape change in the RBC (healthy or infected) can be extremely useful. In case of malarial infection, RBC progressively loses its deformability and tends to occlude the microvessel. In the present study, detailed mesoscopic simulations are performed to investigate the deformation dynamics of an RBC in flow through a constricted channel. Specifically, the manifestation of viscous forces (through flow rates) on the passage and blockage characteristics of a healthy red blood cell (hRBC) vis-á-vis an infected red blood cell (iRBC) are investigated. A finite-sized dissipative particle dynamics framework is used to model plasma in conjunction with a discrete model for the RBC. Instantaneous wall boundary method was used to model no-slip wall boundary conditions with a good control on the near-wall density fluctuations and compressibility effects. To investigate the microvascular occlusion, the RBC motion through 2 types of constricted channels, viz, (1) a tapered microchannel and (2) a stenosed-type microchannel, were simulated. It was observed that the deformation of an infected cell was much less compared with a healthy cell, with an attendant increase in the passage time. Apart from the qualitative features, deformation indices were obtained. The deformation of hRBC was sudden, while the iRBC deformed slowly as it traversed through the constriction. For higher flow rates, both hRBC and iRBC were found to undergo severe deformation. Even under low flow rates, hRBC could easily traverse past the constricted channel. However, for sufficiently slow flow rates (eg, capillary flows), the microchannel was found to be completely blocked by the iRBC.

KEYWORDS

dissipative particle dynamics, mesoscopic simulations, microcirculation, numerical simulations, red blood cell

1 | INTRODUCTION

The hemodynamics of flow through the circulatory system is of immense interest to practitioners.[1] Blood consists of several suspensions that is dominated by the RBCs. These soft deformable cells undergo severe deformation as they pass through the mamallian circulatory system, in particular, arterioles and capillaries.[2] It is well known that healthy RBC is a biconcave semi-discoid cell that can easily squeeze through the capillaries of diameter as small as 3 μm, although its diameter is twice as large.[3] However, the highly deformable RBC can easily become stiffer under disease conditions such as malaria. Thus, a highly flexible, healthy RBC can gradually loose its deformability, during various stages of infection such as ring, trophozoite, and schizont.[4]

In the literature, several attempts have been made to link the deformation dynamics of RBC to its passage characteristics under microcirculation.[5-8] Experimental microfluidic studies have shown the influence of severe constrictions on a cell free layer of blood flow,[5] blockage effects,[6] the progress of infection to rigidity, and the attendant blockage.[7,8] Although the mechanism behind the pathological conditions of iRBC is not well understood, its deformation dynamics at various stages of infection is certainly linked to the cell membrane stiffness, its aggregation dynamics, the transit velocity of the cells, microfluidic channel dimensions etc, where mathematical modeling would be very useful.[9-17]

The modeling and simulation of blood circulation requires an accurate description of the flowing fluid (plasma) with an accurate modeling of geometric and elastic properties of the suspensions such as RBCs, WBCs, and the platelets. A number of efforts have been made to understand the complex rheology of blood via detailed direct simulations of the flow dynamics. It is understood that the mechanics of a microvascular flow is completely different from that of a macrovascular flow due to the confinement effects that occur at microscales.[17] In macroscale flows, the continuum-based 3-dimensional (3D) models are spatially accurate in predicting the flow dynamics in blood vessels. However, these models require more accurate description of the geometry and the boundary conditions. Therefore, when the noninvasive measurements are difficult to obtain, 3D simulations cannot be performed. Alternatively, one powerful route is to perform a comprehensive lumped parameter 0D modeling of the complete circulatory system to understand the hemodynamics.[12-16] These models are based on the traditional electric circuit analogs and useful in tuning patient specific conditions of clinical interest.[18] In fact, outputs from 0D models are often used as inputs for the 1D Navier-Stokes simulations, which are capable of reproducing the arterial hemodynamics. These low-dimensional models are popular owing to their ease with which they predicts physiological flows, without an accurate description for the microvascular wall.[15,16] Most often, these approaches are deemed adequate for capturing the gross behavior of the system and posses significant computational advantage.[18]

Although such models are both useful and practical, of late mesoscopic models have proved to be advantageous in modeling the RBCs suspended in plasma.[19-23] This methodology predominantly involves a particle-based method, viz, dissipative particle dynamics (DPD), which combines the power of molecular level thermal fluctuations by generating the relevant dynamics at useful length and time scales. Pan et al[23] have proposed a low-dimensional model of RBC to simulate blood flows through a constricted microvessel. Using DPD simulations, healthy red blood cell (hRBC) passage characteristics have been simulated in tapered microchannels,[24] converging-diverging pores,[25] through slits,[26] etc. Despite the advantages of particle-based methods in modeling the suspension dynamics, there are various issues such as fluid compressibility effects, numerical convergence, and thermodynamics consistency that can give rise to erroneous pressure and velocity distribution.[27,28] In particular, the DPD simulations in flow through complex geometries suffer from compressibility effects, which leads to particle accumulation in the domain causing anomalous flow behavior.[29] This density fluctuations of particles have been a limitation in using DPD for modeling blood flows in complex geometries. The boundary conditions used for wall modeling is also crucial owing to the controlling of unphysical near-wall density fluctuations. In the present study, wall boundary modeling of Ranjith et al[30] is used in minimizing density fluctuations and for an accurate prediction of velocity field.

A particular form of arterial hardening known as atheroscelerosis is typically responsible for the narrowing of arteries. Such a constriction known as stenosis is responsible for aggravated pathological conditions. Xiao et al[31] have simulated the deformation dynamics of a single RBC in flow through a stenosed microvessel using DPD. They have shown that, with increased bending rigidity of the membrane, the RBC becomes less deformable and takes longer transient time. The infected RBC was modeled using higher bending stiffness, while surface-to-volume ratio (initial stress free shape) and the modulus of elasticity are also important parameters that influence the deformation dynamics of RBC under stenosed conditions.[32,33] The microvascular occlusion of a narrow vessel by a single infected red blood cell (iRBC) is shown using moving particle semi-implicit method.[34] The blockage of tapered microvessel by an iRBC at scizont stage was simulated using smoothed particle hydrodynamics.[35] Vahidkhah and Fatouraee[36] reported the

deformation and aggregation of 2 RBCs in a stenosed microchannel. Nakamura and Wada[37] studied the effect of shear stress on the RBC membrane for a better estimation of hemolysis. They have shown that the RBC motion and the shear stress induced on the membrane are not consistent under stenosed condition of the microvessel, necessitating the need to model hemolysis. However, in their study, cell membrane of the RBC was modeled using linear springs, and the thermal fluctuation of biological cells were completely ignored. Recently, Vahidkhah et al[17] presented a 3D simulation study showing the various aspects of flow conditions in stenosed microvessels. In particular, they found that increase in relative viscosity near the stenosis due to blockage is indeed a function of interactions between the RBCs and the vessel wall.

The deformation dynamics of RBCs have been well investigated by experimental, theoretical, and numerical means. The 2-dimensional (2D) models have been used in a number of studies to represent the fluid dynamical phenomena involving RBC membrane dynamics, viz, proximity to boundaries, membrane dynamics modes, and cell deformation.[38-43] A potential limitation in most of the 2D RBC models is that it does not experience the out-of-plane tumbling motion, which is evident in 3D simulation.[20,44] This discrepancy is related to simulations of the tank-treading motion of RBC membrane in pure shear flows. To overcome this discrepancy, Finken et al[45] adapted a concept of elastic energy barrier associated with the RBC membrane. If it can be overcome by the hydrodynamic forces, the membrane performs tank-treading motion. If it is not enough, the membrane performs tumbling motion. The energy barrier can be associated with the nonuniform 3D meshes of RBC membrane.[22,46] In some 2D simulations, an extra elastic energy term is used for capturing the different deformation modes of RBC in pure shear flow.[47] Apart from that, 2D models of the RBC membrane has been shown to recover many of the 3D results in Poiseuille flow.[44,48,49] A detailed comparison of 2D and 3D simulation of blood flow using DPD can be found in Müller.[50] His work depicts a clear qualitative similarity between the 2D and 3D simulations in terms of hematocrit, shear rate, and the margination characteristics of RBCs. The 2D RBC membrane is built using 50 DPD particles, similar to the model presented in this study. In 2D, the surface area is replaced by a line length, with DPD particles, and the sphere volume is replaced by the circle area A. The low-dimensional model proposed by Pan et al[23] can also be fitted to produce the nonlinear elastic deformation of RBC membrane as measured in optical tweezers experiment. Here, we consider a 2D simulation due to its enormous computational advantages and motivated by the fact that in several circumstances, a 2D study captures the 3D results to a good accord.[49,51-54] A deeper understanding of the interplay among fluid forces, elastic response, and dynamics of RBC membrane will certainly elucidate about the blocking effects. In this regard, a 2D model is more useful in understanding the relationship between elastic response and dynamics of the RBC membrane due to its less complexity compared to a 3D simulation. It should be pointed out that, although 3-dimensional simulations have been attempted in the literature,[55-57] systematic 2D simulations are useful to understand the RBC-plasma interactions and facilitate better understanding of the passage and blockage characteristics in a simple manner.

In view of above-cited literature, we notice that occlusion characteristics of iRBC in microchannel have not received adequate attention. Although the viscous forces play a vital role, detailed deformation dynamics of hRBC as well as iRBC is not well addressed, as they pass through 2 different types of microchannels, viz, (1) tapered microchannel and a (2) stenosed-type microchannel. Specifically, the interaction between fluid forces and elastic forces of the RBC on passage and blockage characteristics in stenosed microchannel is not available in the literature. Moreover, pathogenesis of the iRBC invariably starts from a single-cell infection, and it would be highly pertinent to perform single-cell analysis rather than its behavior in bulk. Therefore, clearly, we see that it is of utmost importance to understand the deformation dynamics of a single RBC in highly confined channels.

The paper is organized as follows. In Section 2, a brief review of finite-sized dissipative particle dynamics (FDPD) method and the discrete particle model of RBC is presented. The implementation aspects of our instantaneous wall boundary (IWB) modeling is also presented. In Section 3, we validate the RBC mechanics by mimicking the optical tweezers experiment. This section also presents validation for the microchannel flow simulations against the standard computational fluid dynamics (CFD) studies. The motion of hRBC in a tapered channel is compared with that of experimental studies. The FDPD simulations analyzing the rheological characteristics of deformed blood cells (both hRBC and iRBC) under tapered and stenosed microchannel flows is presented. The paper ends with a brief summary and conclusions in Section 4.

2 | FDPD METHODOLOGY

In this section, we briefly summarize the FDPD formulation along with a 2D discrete cell model of RBC in conjunction with a novel methodology for implementing the boundary condition.

2.1 | Fluid model

The FDPD particles simulate both the solvent and the dispersed cells and are assumed to have mass m and mass moment of inertia $\boldsymbol{I}$. The particles obey linear momentum balance given by

$$m\frac{d\boldsymbol{v}_i}{dt} = \boldsymbol{f}_i, \tag{1}$$

where $\boldsymbol{v}_i$ is the velocity and the $\boldsymbol{f}_i$, the total force on the ith particle. The angular momentum balance equation for the ith particle is

$$\boldsymbol{I}\frac{d\boldsymbol{\omega}_i}{dt} = -\sum_{j\neq i}\lambda_{ij}\boldsymbol{r}_{ij}\times\boldsymbol{f}_{ij}, \tag{2}$$

where $\boldsymbol{\omega}_j$ is the angular velocity and $\boldsymbol{f}_{ij}$ is the force excerted on the ith particle by the jth particle. The distance between particles i and j is given by $\boldsymbol{r}_{ij} = \boldsymbol{r}_i - \boldsymbol{r}_j$. The position, linear, and angular velocity of each particle are determined by the total total force exerted by the surrounding particles within a finite cutoff radius, r_c. The contributions of 4 types of forces (central, C; transnational, T; rotational, R; and stochastic, S) are considered:

$$\boldsymbol{f}_{ij} = \boldsymbol{f}_{ij}^C + \boldsymbol{f}_{ij}^T + \boldsymbol{f}_{ij}^R + \boldsymbol{f}_{ij}^S. \tag{3}$$

The force on the ith particle may also include external forces ($\boldsymbol{f}^E$) from forces such as gravitational, magnetic, or electroosmotic. Thus, the total force on the ith particle is due to the effective force exerted by the neighbors as well as the external force given by

$$\boldsymbol{f}_i = \sum_{j\neq i}\boldsymbol{f}_{ij} + \boldsymbol{f}^E. \tag{4}$$

The central nonconservative repulsive force acting along the line connecting particle centers is given as

$$\boldsymbol{f}_{ij}^C = a_{ij}\Gamma(r_{ij})\boldsymbol{e}_{ij}, \tag{5}$$

where a_{ij} is the repulsion parameter, $r_{ij} = |r_{ij}|$, and $\boldsymbol{e}_{ij} = \boldsymbol{r}_{ij}/|r_{ij}|$ is a unit vector. An appropriate weight function, $\Gamma(r_{ij})$, is selected such that the conservative force vanishes linearly at the limiting value $r_{ij} = r_c$. Most DPD simulations take $\Gamma(r_{ij})$ to be

$$\Gamma(r_{ij}) = \begin{cases} \left(1-\dfrac{r_{ij}}{r_c}\right), & \text{if} \quad r_{ij} < r_c, \\ 0, & \text{otherwise.} \end{cases} \tag{6}$$

The translational force is assumed to have central and noncentral dissipative components given by

$$\boldsymbol{f}_{ij}^T = -\gamma_{ij}^{\parallel}w^2(r_{ij})(\boldsymbol{v}_{ij}.\boldsymbol{e}_{ij})\boldsymbol{e}_{ij} - \gamma_{ij}^{\perp}w^2(r_{ij})[\boldsymbol{v}_{ij} - (\boldsymbol{v}_{ij}.\boldsymbol{e}_{ij})\boldsymbol{e}_{ij}], \tag{7}$$

where $\gamma_{ij}^{\parallel}$ and $\gamma_{ij}^{\perp}$ are longitudinal and transverse dissipation coefficients, respectively. This frictional force attempts to reduce the relative velocity $\boldsymbol{v}_{ij} = \boldsymbol{v}_i - \boldsymbol{v}_j$ between particles in both directions. The rotational dissipative force is taken to be of the form

$$\boldsymbol{f}_{ij}^R = -\gamma_{ij}^{\perp}w^2(r_{ij})[\boldsymbol{r}_{ij}\times(\lambda_{ij}\boldsymbol{\omega}_i + \lambda_{ji}\boldsymbol{\omega}_j)]. \tag{8}$$

A stochastic force, which accounts for the lost degrees of freedom of individual molecules in the coarse graining process, is taken to be

$$\boldsymbol{f}_{ij}\Delta t = w(r_{ij})[\sigma_{ij}^{\parallel}tr[d\boldsymbol{W}_{ij}]\frac{1}{\sqrt{d}}\boldsymbol{I} + \sqrt{2}\sigma_{ij}^{\perp}d\boldsymbol{W}_{ij}^A].\boldsymbol{e}_{ij}, \tag{9}$$

where Δt is the time step, $d=2$ for 2D simulations, and $tr[d\mathbf{W}_{ij}]$ is the trace of symmetric-independent Wiener increment matrix $d\mathbf{W}_{ij}$ and while $d\mathbf{W}_{ij}^A$ is its anti symmetric part. According to the fluctuating dissipation theorem, the random and dissipation coefficients are correlated by $\sigma_{ij}^{\parallel} = \sqrt{2k_B T \gamma_{ij}^{\parallel}}$ and $\sigma_{ij}^{\perp} = \sqrt{2k_B T \gamma_{ij}^{\perp}}$. The stochastic forces and the dissipative forces together act to maintain a constant temperature during the simulations. w_{ij} is given by

$$w(r_{ij}) = \begin{cases} \left(1-\dfrac{r_{ij}}{r_c}\right)^k, & \text{if } r_{ij}<r_c, \\ 0, & \text{otherwise.} \end{cases} \tag{10}$$

Following Fan et al,[58] the value of k is taken to be equal to 0.25 in the present simulation.

2.2 | The RBC model

The RBC is modeled using finite-sized DPD as a ring of 50 particles connected by worm-like chain (WLC) springs. Pan et al[23] proposed a low-dimensional model of RBC, with 10 particles connecting through WLC springs. Although the present formulation is similar to that of Pan et al,[23] we introduce an additional penalty term for the area conservation of the membrane.[38,59] The initial shape of the RBC model used in the simulation is presented in Figure 1. A close-up view of WLC spring model of RBC membrane depicts the angle θ_{ijk} between adjacent springs. The WLC spring force is an interpolation formula that describes the extension r_{ij} of WLC chain with maximum allowable length l_0 for each spring and persistence length l_p, given by

$$f_{WLC} = \frac{K_B T}{4l_p} \left[\frac{1}{\left(1-\frac{r_{ij}}{l_0}\right)^2} - 1 + \frac{4r_{ij}}{l_0} \right]. \tag{11}$$

The persistence length is a basic mechanical unit that quantifies the stiffness of a polymer. For a polymer segment that is shorter than the persistence length, the molecules tend to behave like a flexible rod. A repulsive force similar to Equation 5 is also applied between the cell particles to counter the purely attractive WLC forces to enable the RBC membrane in equilibrium. Since a typical cell has bending resistance, the following bending potential is introduced:

$$U_b = k_b\left(1-\cos(\theta_{ijk})\right), \tag{12}$$

where k_b is the bending rigidity coefficient and θ_{ijk} is the angle between 2 adjacent springs. The bending force on the jth particle is derived as
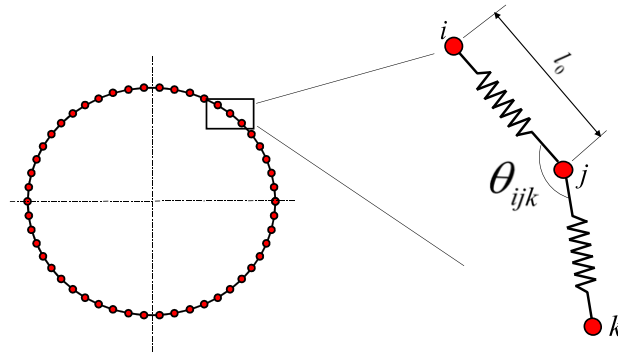
$$f_b = -\frac{\partial U_b}{\partial r_j}. \tag{13}$$

FIGURE 1 Two-dimensional red blood cell membrane model, with a close up view of the worm-like chain spring model. θ_{ijk} refers to the angle made by 2 adjacent springs ij and jk at the junction j

Global area constant is introduced as a penalty function. Area potential is given by

$$U_a = \frac{k_a(A - A_0)^2}{2A_0^2},$$ (14)

where A is the instantaneous area and A_0 the desired enclosed area. k_a is area coefficient. The force f_a can be obtained from

$$f_a = \frac{\partial U_a}{\partial r_j}.$$ (15)

Finally, by combining Equations 11, 13, and 15, the total force acting on each DPD particle of the cell membrane is obtained.

2.3 | Boundary conditions

In this section, we briefly describe the implementation of a novel no-slip boundary condition for solid wall boundary. One popular approach to model wall boundaries is by introducing frozen layers of wall particles. However, this approach results in high-density fluctuations closer to the wall. For controlling such undesirable near-wall density fluctuations, extra care should be taken in modeling the wall boundaries, within the FDPD framework. In modeling viscous fluid flow through constricted geometries, the FDPD method may develop pseudocompressibility effects, which results in abnormal velocity field in such cases. Also, in flow through severe constrictions, it may be possible that numerical convergence is effected.[29] The study of Ranjith et al[30] have introduced momentary freezing of these particles on the wall to achieve an IWB. This approach was shown to have a remarkable reduction in the density fluctuations closer to the wall. Furthermore, this approach has been successfully used to model the flexible membranes inside a flow field.[60] Thus, in this formulation, there are no fixed wall particles used to model a solid boundary. Instead, any fluid particle that comes within the cutoff radius of a solid boundary will interact with an instantaneous frozen particle (IFP). This method is advantageous in controlling the fluid-solid conservative force, which in turn helps in suppressing the near-wall density fluctuations. The conservative force can be expressed as

$$\boldsymbol{f}_{fm}^{cons} = a_{fm}\Psi(r_{fm})\boldsymbol{e}_{fm},$$ (16)

where a_{fm} is the repulsion parameter between the fluid (referred by f) and solid wall (referred by m) particles, $r_{fm} = |\boldsymbol{r}_{fm}|$, and unit vector is $\boldsymbol{e}_{fm} = \boldsymbol{r}_{fm}/r_{fm}$. To achieve minimal near-wall density fluctuations, proper tuning of the parameter, $\Psi(r_{fm})$ is required such that the function is stiff near the wall and softer gradually away from the wall. In this regard, an appropriate function is chosen as

$$\Psi(r_{fm}) = \begin{cases} \kappa\left(\dfrac{1-(\frac{r_{fm}}{r_c})^3}{\kappa + (\frac{r_{fm}}{r_c})^3}\right), & \text{if} \quad r_{fm} < r_c, \\ 0 & \text{if} \quad r_{fm} > r_c. \end{cases}$$ (17)

For $\kappa = 0.1$, the plot of the function is shown in Figure 2A. It can be noticed that the required conditions are fulfilled for this value of κ, which is used in all further simulations. In the present study, this approach has been further extended to model inclined and curved boundaries. The particle interaction with boundaries is shown in Figure 2B,C, where the fluid particle within the cutoff radius near the wall interacts with a single-wall particle, which is instantaneously assumed to be located at the shortest distance either on an inclined wall or a curved boundary. If a particle having spatial coordinates (x_p, y_p) comes within the cutoff radius of the solid wall, it will interact with an instantaneous wall particle (x_{w1}, y_{w1}) through particle-wall conservative, dissipative, and random forces. The difficulty in applying the IWB is to find the position of the IFP accurately at each time step. For an inclined plane, the position of the IFP is calculated analytically using the following relation:

$$x_{w1} = \frac{x_p/m + y_p + mx}{m + 1/m}, y_{w1} = m\left(\frac{x_p/m + y_p - y/m}{m + 1/m}\right),$$ (18)
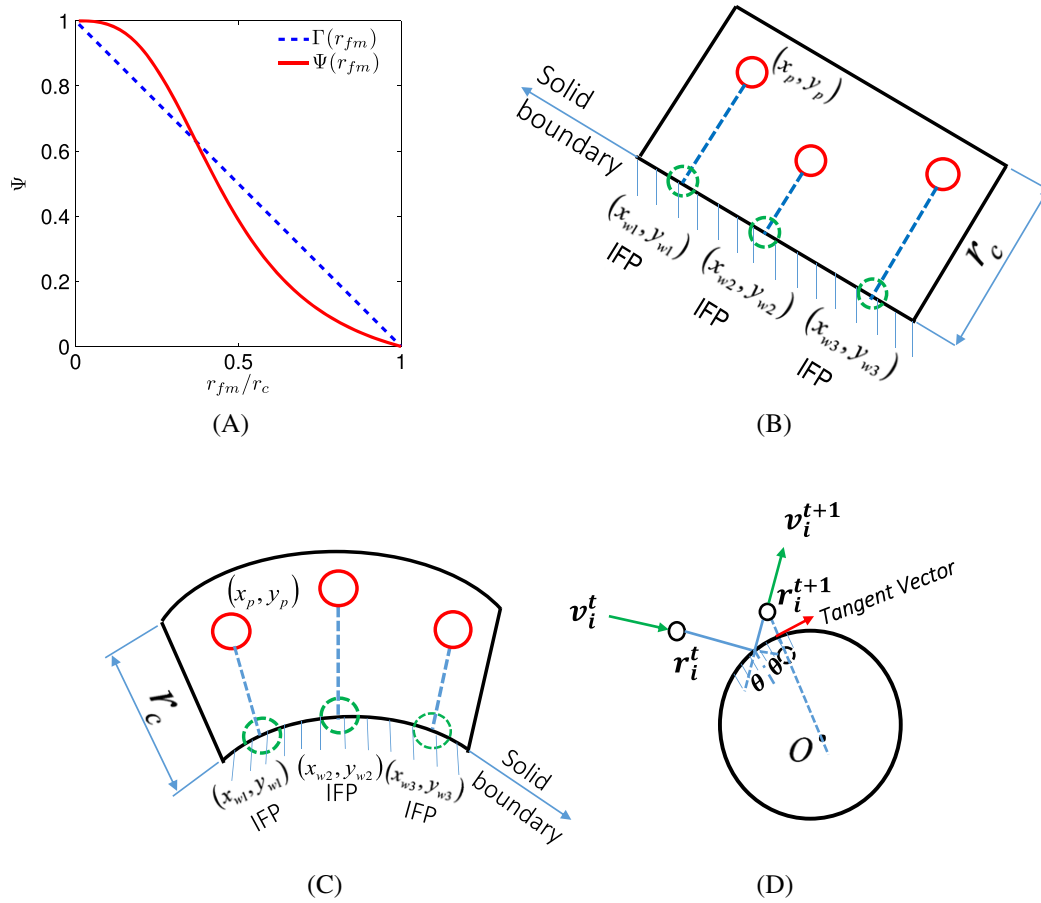
FIGURE 2 A, Plot of the conservative weight function $\Psi(r_{fm})$ between the fluid and material wall particle in comparison with the weight function for conservative force between fluid particles, each fluid particle within r_c from the solid wall interacts with its corresponding instantaneous frozen particle (IFP); B, straight inclined boundary; C, curved wall boundary; and D, specular reflection on a circular boundary

where m is the slope of the inclined plane and (x, y) is the coordinate of the point through which inclined wall would pass through. For a semicircular wall (stenosed condition), IFP is easily identified by noticing that the normal to a circle at any point always passes through the centre of the circle. The fluid particle escaping from the computational domain is reflected back from the wall. The interaction between fluid and wall particles are considered to be elastic and specular. In specular reflections, the velocity component tangential to the wall does not change, while the normal component is reversed. As shown in Figure 2D, an instantaneous tangent is found at the wall for each particle that escapes the computational domain. The plasma particle is then reintroduced into the simulation domain by reflecting from the local tangent. The position of the instantaneous tangent is calculated numerically using Newton-Raphson method.[61] Furthermore, the periodic boundary conditions are applied at the inlet and outlet.

2.4 | Computational details

Different values corresponding to various FDPD parameters used in the present simulation are mentioned in this section. The cutoff radius r_c is chosen as unity, while the system temperature is maintained constant at $K_B T = 0.0945$. The dissipation parameters is chosen to be $\gamma = 4.5$ and the stochastic force coefficient $\sigma = 0.922$ for both fluid-fluid and fluid-wall particle interactions. Usually, the conservative force coefficient (a_{ij}) is calculated using the relation $\dfrac{75 K_B T}{\rho}$.[62] In our simulation, a higher value is used to control the density fluctuation in the axial direction due to geometric constriction.[63] All the fluid and boundary particles are assumed to be of the same size so that the size parameter is $\lambda_{ij} = \lambda_{ji} = 0.5$. A constant driving force is applied to simulate the dynamical evolution. The magnitude of this force is varied from 0.02 to 0.06 to obtain different flow rates. The temporal evolution of particle

positions is obtained by integrating the momentum equations using the modified velocity Verlet scheme with a time step size of order $O(10^{-3})$.

3 | RESULTS AND DISCUSSION

3.1 | Validation studies

Detailed validation of FDPD formulation is presented in this section. This method is shown to capture hydrodynamics of suspensions accurately.[64,65] The FDPD model validation of RBC mechanics and dynamics is discussed below.

3.1.1 | RBC Mechanics

It is well known that optical tweezers experiment of a single RBC exemplifies its deformation characterstics.[66] In the present FDPD simulation, this is emulated to achieve a stable minimum energy state of RBC membrane, without enforcing the area penalty. A ring of 50 DPD particles are used to model the membrane of the RBC. For the purpose of mechanical testing, one membrane particle is fixed, and particle on the opposite side is gradually pulled with an axial force. The resulting increase in the axial diameter of the membrane with an attendant decrease in transverse diameter is monitored. The variation of axial and transverse diameters of RBC as a function of applied axial force is presented in Figure 3, and compared against the well-known experimental findings of Suresh et al[66] as well as the 3D simulation of Hosseini and Feng.[32] A reasonably good agreement can be observed between the present simulation and the 3D simulations and experimental results for the hRBC. Similarly, the iRBC data refer to comparison for a schizont state. Thus, the membrane properties associated with the healthy and infected RBC are well replicated in the DPD framework. The modulus of elasticity for a hRBC is taken to be 6 μN/m. The value of l_0 and conservative force coefficient a are chosen to be 0.45 and 50.0, respectively. The bending stiffness k_b is adjusted such that a good agreement could be obtained with the experiments. Recently, it was observed that the presence of the rigid merozoites results in overall loss of deformability of the RBC.[32] However, the influence of merozoites on the mechanical properties is still unclear. Therefore, following Pan et al,[23] we elevate the membrane properties in the modeling of iRBC compared to hRBC. The parameters used in the simulation are summarized in Table 1.

Initial diameter of the RBC is taken to be $D_r = 6.1r_c$. The reduced area parameter is defined as $s^* = \dfrac{4A_0}{\pi D_r^2}$, where A_0 is the desired enclosed area of the RBC. The area conservation force is applied to get the biconcave shape of hRBC at $s^* = 0.481$, and the iRBC was found to swell into an elliptic shape as shown in Figure 4. These 2 initial shapes are fixed through out the simulation to represent hRBC and iRBC, respectively.
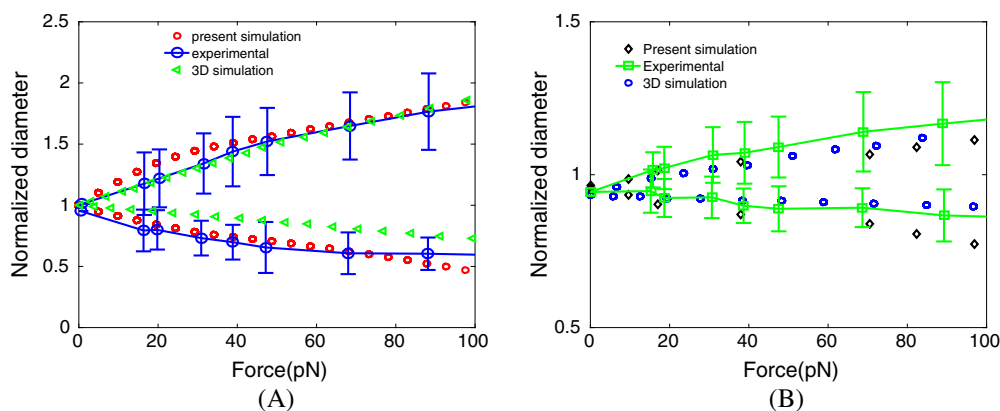

FIGURE 3 Axial and transverse deformation of red blood cell (RBC) diameter against stretching force, comparison against experimental observation[66] and numerical results[32] for A, healthy RBC and B, infected RBC at schizont state

TABLE 1 Parameters used for hRBC and iRBC refers to healthy and infected cell, respectively[a]

Parameters	hRBC	iRBC
N_c	50	50
a	50.0	275.0
l_0	0.45	0.45
λ_p	0.0067	0.00067
k_b	$50 K_B T$	$500 K_B T$
k_a	$22326 K_B T / D_r^2$	$223260 K_B T / D_r^2$

[a]The latter refers to the properties of schizont state.

Abbreviations: hRBC, healthy red blood cell; iRBC, infected red blood cell.

(A)   (B)
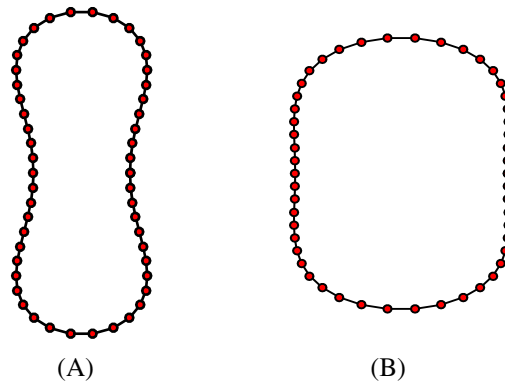
FIGURE 4 The shape of A, healthy red blood cell (RBC) and B, infected RBC after applying the area penalty function. The latter refers to a schizont state of an infected RBC

3.1.2 | RBC dynamics

The spatio-temporal dynamics of a single hRBC in plasma flow is considered. Here, the dynamics of RBC and its resulting deformation in planar Poiseuille flow and in shear flow is numerically simulated. It was observed in earlier studies that hRBC deforms into a parachute-like shape from an initial biconcave shape in Poiseuille flow.[48,67,68] An hRBC with an initial biconcave shape is kept in the middle of a microchannel of width $10 r_c$. Because of parabolic nature of the Poiseuille flow, the solvent plasma pushes the hRBC at the center, resulting in the forward bulge of the RBC. Figure 5 depicts the shape transition in the RBC from an initial biconcave to a parachute-like shape. In fact, the velocity of the neighboring plasma particles and the initial position of the RBC, as well as the width of the microchannel, play a crucial role in the shape transition of RBC. A phase diagram depicting flow rate (Q) on the abscissa against reduced area (s^*) on the ordinate is presented in Figure 6. It can be noticed that, as the flow rate increases, hRBC assumes parachute-like shape for s^* below 0.6. However, above this critical value of s^*, hRBC attains a bullet-like shape. Furthermore, a negative curvature of the cell membrane at the rear is observed below $s^* = 0.7$. These shapes are observed under symmetric parabolic flow by placing the cell exactly at the center of the channel. However, when the hRBC was placed asymmetrically (with a bias towards the upper wall), an asymmetric slipper-like shape of the RBC was noticed (see Figure 7). Interestingly, RBC has a tendency to migrate towards the center of the cell. Thus, shape transition from slipper (asymmetric) to parachute-like (symmetric) shape was observed because of the cell migration towards the center

FIGURE 5 The shape changes in a single healthy red blood cell as it moves under Poiseuille flow at nondimensional times $t = 0, 25, 50, 75, 100, 125, 150, 175$. Gradual shape transition from an initial biconcave to axisymmetric parachute-like shape can be noticed
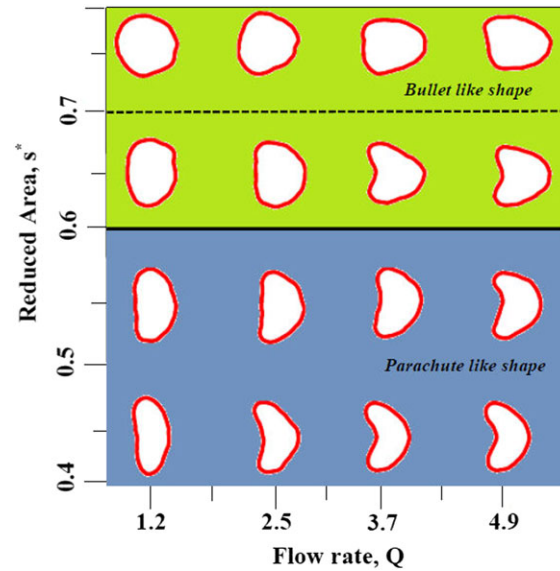
FIGURE 6 Phase diagram in the plane of reduced area against flow rate. Shape evolution of healthy red blood cell (hRBC) is shown. The horizontal solid line differentiates the bullet-like shape and parachute-like shape of hRBC. The dashed line represents the boundary below, which the bullet-like shape has a negative curvature at the rear
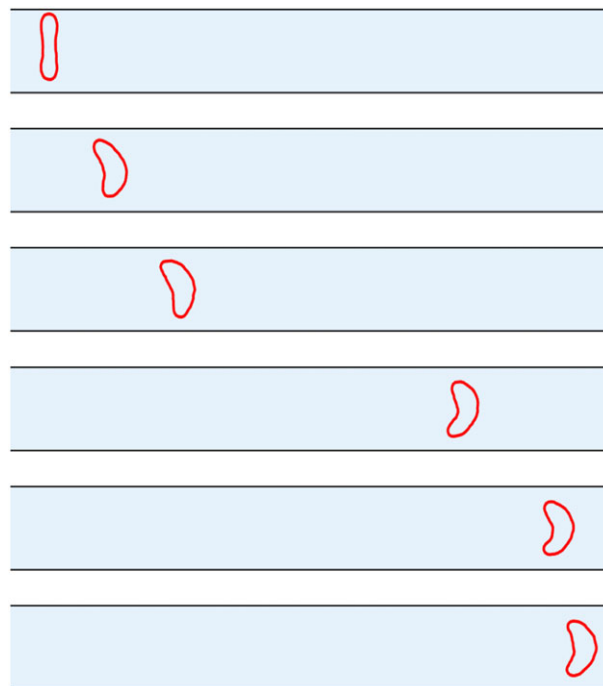

FIGURE 7 Temporal evolution of a healthy red blood cell (RBC) membrane shape initially placed closer to the upper wall of the microchannel is shown. The shape transformation from initial biconcave to asymmetric slipper-like shape is observed. Finally, symmetric parachute-like shape can be noticed as RBC migrates towards the center of the cell

of the microchannel. The steady state RBC deformation for different values of reduced area is presented in Figure 8 and compared with the results of Kauoi et al.[48] A close agreement between different mode shapes of RBC membrane can be noticed.

The transient deformation of a circular-shaped RBC in a pure shear flow is simulated. The temporal evaluation of Taylor deformation parameter is calculated and compared against the 3D Navier-Stokes–based simulation of Sui et al.[46] The Taylor deformation parameter is defined as $D_{xy} = \dfrac{L-W}{L+W}$, where L and W are the major and the minor radii of the RBC, respectively. The capillary number, defined as $\dfrac{\mu \dot{\gamma}}{E_s}$, is calculated to be 0.15 based on the DPD parameters. As
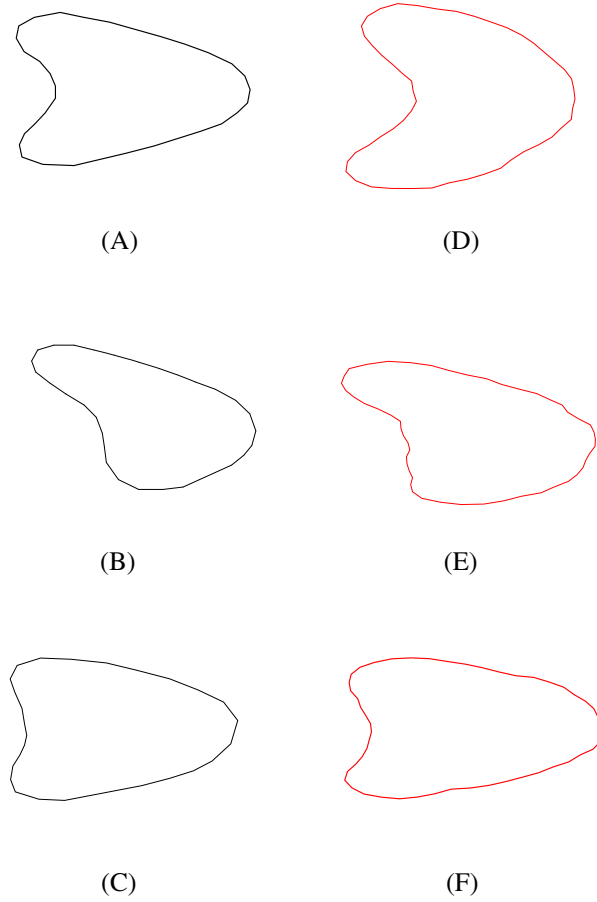
FIGURE 8 Comparison of deformed red blood cell shape in Poiseuille flow: A, parachute-like; B, slipper-like; and C, bullet-like shape taken from Kaoui et al[48] and D, parachute-like; E, slipper-like; and F, bullet-like shape in present finite-sized dissipative particle dynamics simulation. These shapes are obtained by varying the reduced area parameter. The parachute and slipper shapes are obtained for s^* value of 0.481, while bullet-like shape is observed for s^* value of 0.75

shown in Figure 9, a good agreement is observed between the current 2D and the 3D simulation of Sui et al.[46] Further, we examine the tank-treading characteristics of a biconcave-shaped red blood cell in a simple shear flow. For sufficiently higher shear rates, the cell deforms from its initial biconcave shape to an ellipsoidal shape. The cell membrane rotates continuously in simple shear flow, which is popularly known as tank-treading motion. This motion is quantified by the tank-treading frequency f, defined as the inverse of the period (1/T). Experimental results[69] indicate that the frequency, f, scales with the shear rate, $\dot{\gamma}$, to be in the range $f/\dot{\gamma} = 0.02$ to 0.038. But in our present simulations,
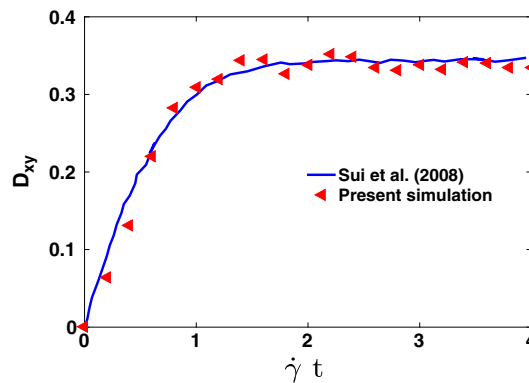
FIGURE 9 Temporal evolution of Taylor deformation parameter of a healthy red blood cell at $Ca = 0.15$ compared against the 3D simulation of Sui et al[46]

corresponding value was found to be $f/\dot{\gamma} = 0.167$, which is significantly higher than what is expected. This discrepancy between the experiments and computations is attributed to the nature of the present 2D simulations, while experiments are always 3D. In fact, Hosseini et al[70] have pointed out that, in a Stokes flow, a 2D solid cylinder rotates with a period of $2/\dot{\gamma}$ while a sphere has a much longer period of $4\pi/\dot{\gamma}$.[71] Hence, the factor of 2π was attributed between 2D computation and 3D measurements. Nevertheless, the present 2D computations can be said to be in good agreement with the values found in the 2D simulations of Hosseini et al.[70]

3.1.3 | Flow through a constricted microchannel

We further investigate 2 different types of microchannels, viz, (a) a tapered channel and (b) a stenosed channel. The latter is particularly chosen, based on recent numerical simulations, which mimic microvascular stenosis.[36] The schematic of the tapered flow domain is shown in Figure 10, where D is the initial channel width and h is the width of constricted region. Present simulations are conducted for an h/D ratio of 0.35. The normalized velocity at 3 different sections is extracted and compared with a grid independent ANSYS Fluent simulations as shown in Figure 10. A good comparison between FDPD results and the finite volume method can be noticed. However, the near-wall density fluctuations were found to be negligible (see Figure 10D). Axial density variation is generally observed in irregular geometries such as severe constricted microchannel, which may sometimes affect the streamwise velocity profile of the flow field. This density variation with the present IWB model is reduced to almost less than 10%, which is a
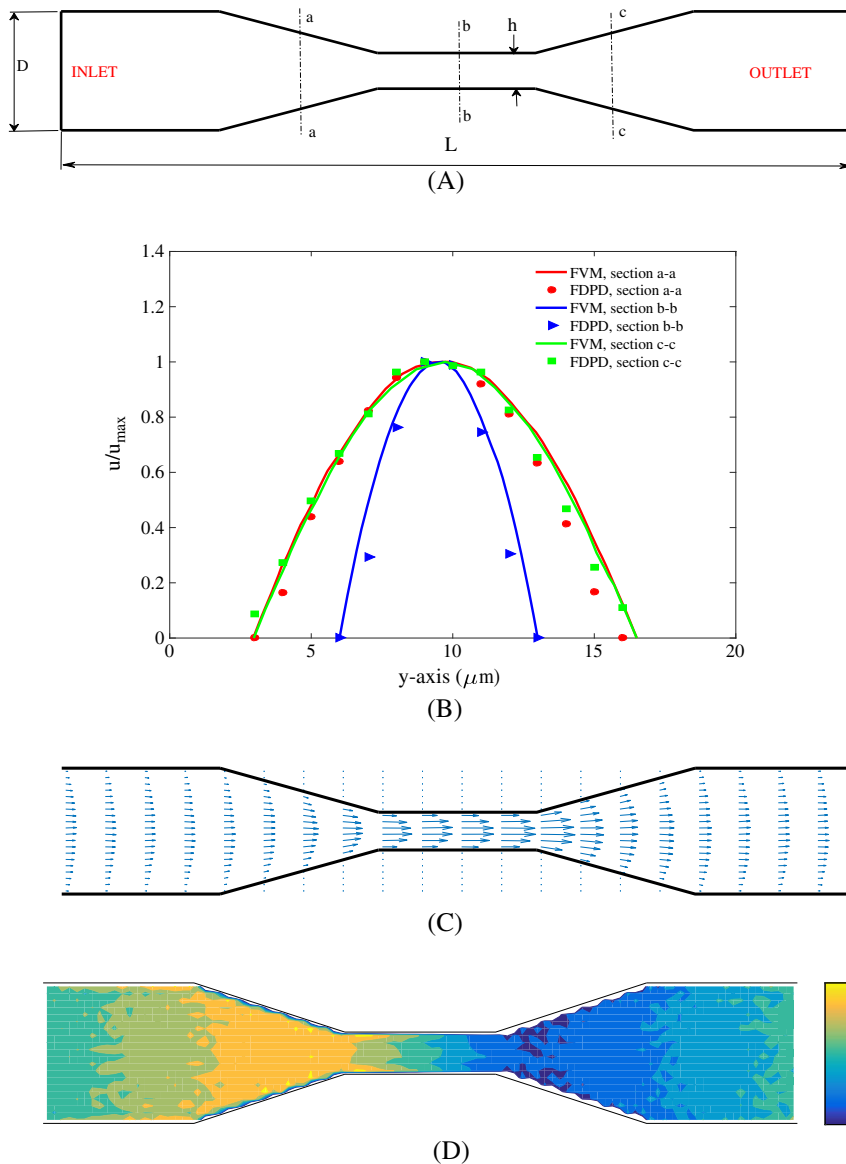
(A)

(B)

(C)

(D)

FIGURE 10 Comparison of axial velocity along channel cross section (y-axis) in a tapered channel: A, schematic of tapered microfluidic channel with $h/D = 0.35$ and length $L = 100 r_c$. Sections a-a, b-b, and c-c where velocity profiles are obtained: B, axial velocity profiles of the finite-sized dissipative particle dynamics (FDPD) simulations are compared against finite volume method (FVM) results; C, time averaged velocity vector plot; and D, normalized density contour plot

significant improvement for a particle-based method. Also, this small variation does not significantly alter the flow field, which can be inferred from the velocity vector field (see Figure 10C). Following the work of Quinn et al,[24] dynamics of hRBC flowing through a tapered microchannel of width $4r_c$ is investigated. The deformation dynamics of hRBC through the tapered microfluidic channel against the experimental visualization of Quinn et al[24] is presented in Figure 11. Figure 11D presents the variation of longitudinal axis of the cell measured at the center of the constricted channel, with different width of constrictions. The present 2D simulations predict a little less deformation compared with the experimental study. The difference between 2D and 3D simulations is about 5% to 10%. The FDPD simulations present a reasonably good correspondence with the earlier studies reported in the literature.

A symmetric stenosed microchannel is shown in Figure 12, with a constricted semicircular cross section. The length of the microchannel is $L = 100r_c$ and diameter $D = 20r_c$. The area ratio is defined as the ratio of the area at the section of maximum constriction to the main channel diameter. Simulations are conducted for an area ratio of approximately 0.4. Figure 12 presents the axial velocity profiles at 3 different sections, which are compared against standard finite volume method–based simulations. The velocity vector plot and the normalized density map are shown in Figure 12. Almost uniform density distribution can be noticed with less than 10% variation, which typically occurs because of the severe constricted nature of the microchannel. Initially, the system temperature is taken to be constant at $k_B T = 0.0945$. The DPD parameters are chosen such that the dissipative and random forces act as a thermostat to maintain the constant temperature as shown in Figure 13. The average system temperature in both cases are in close agreement with the initial system temperature.

3.2 | FDPD simulation of healthy and infected RBC

In this section, 2D simulation on the deformation dynamics of a healthy and an infected RBC through a constricted channel is presented. Two different types of flow domains with rigid walls considered are (a) a tapered channel and (b) a stenosed microchannel. The motion of single hRBC as well as an iRBC through 2 types of microfluidic channels is discussed.
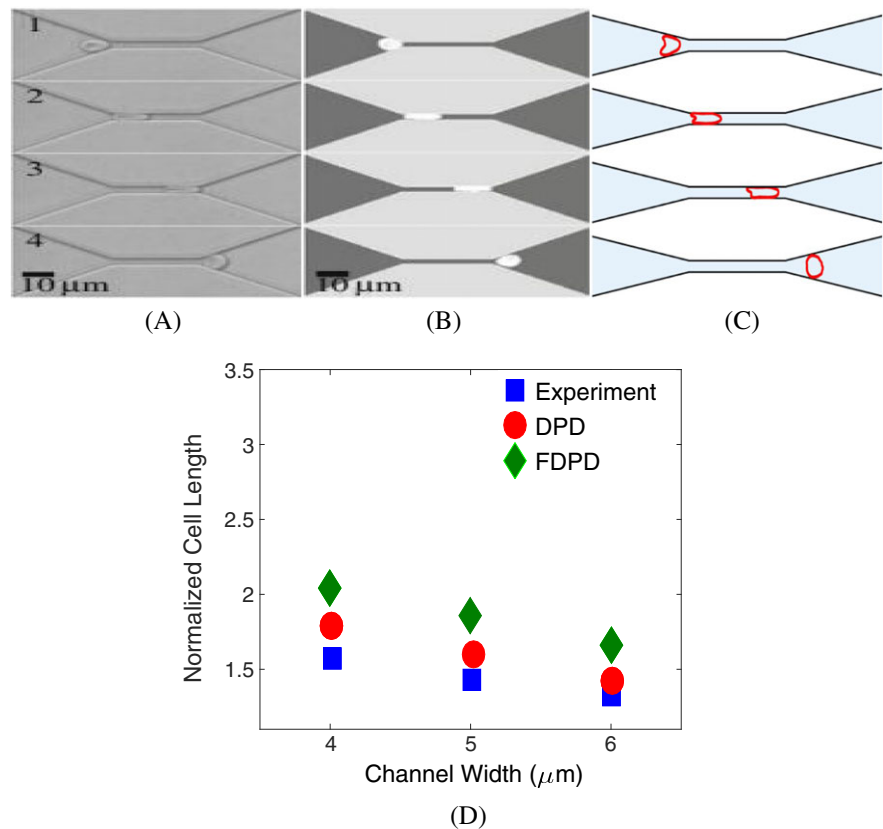

FIGURE 11 Shape transformation of red blood cell (RBC) traversing through a tapered channel: A, experimental visual; B, dissipative particle dynamics (DPD) simulation of RBC traversing through a $4r_c$ width, $30r_c$ long, and $2.7r_c$ height channel[24] (3D simulation); C, finite-sized dissipative particle dynamics (FDPD) simulation of RBC traversing through a $4r_c$ width, $30r_c$ long tapered channel (2D simulation): D, variation in cell lengths measured axially at the centre of tapered channel with varying widths
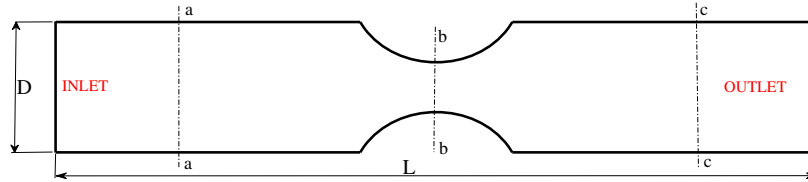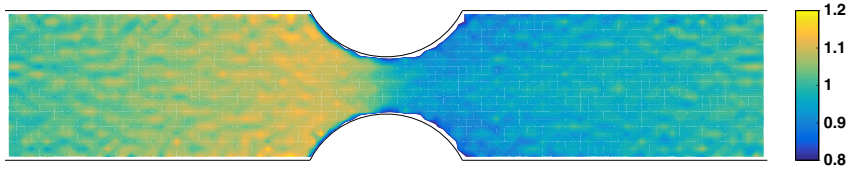
(A)
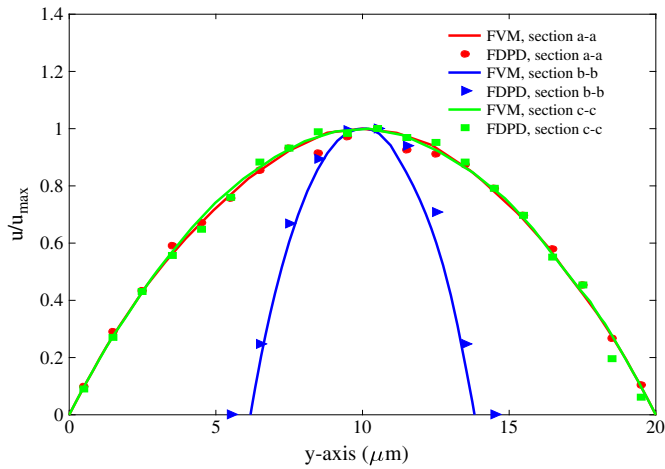
(B)
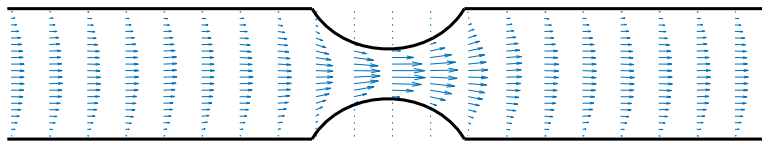
(C)

(D)

FIGURE 12 Comparison of axial velocity against channel width (*y*-axis) in a stenosed channel. A, Schematic of stenosed microfluidic channel of length $L = 100r_c$ and $D = 20r_c$ with about 40% area constriction. Sections a-a, b-b, and c-c where velocity profiles are obtained: B, axial velocity profiles of the finite-sized dissipative particle dynamics (FDPD) are compared against the finite volume method (FVM) results; C, time averaged velocity vector plot; and D, the normalized density contour plot
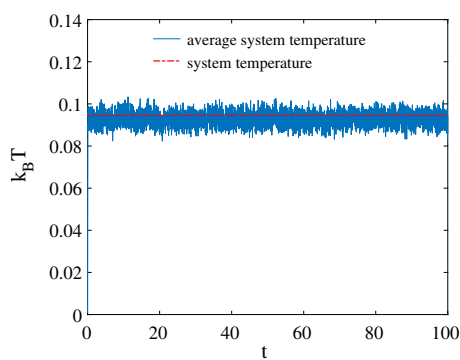
(A)
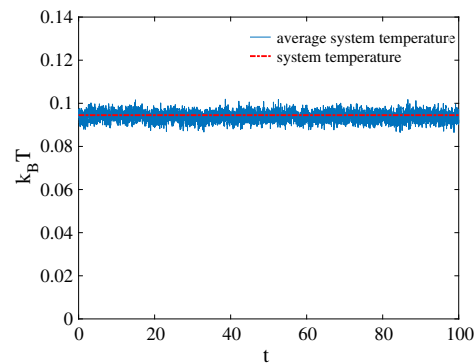
(B)

FIGURE 13 Variation of domain temperature with time, *t*: A, tapered microchannel of width 6 μm; B, stenosed microfluidic channel with 40% constriction

3.2.1 | RBC motion through tapered microchannel

The dynamics of hRBC and iRBC (the latter with a schizont state of malarial infection) through a tapered microchannel is presented. To start with, the width of the channel h is varied to study the passage/blockage characteristics of hRBC and iRBC as they move past the constriction. The width of the capillary is varied from $h = 4r_c$ to $6r_c$. Initially, hRBC moves along the axial direction because of the motion of plasma particles. The hRBC starts deforming as it passes through the microcapillary. The hRBC and iRBC motion in a capillary of width $h = 6r_c$ is shown in Figure 14. While the RBC passes through, it deforms into parachute-like shape, the shape deformation of iRBC can be noticed to be much less, and hence, it takes a much longer time compared with hRBC. There is a narrow gap between the cell and capillary wall in case of hRBC. The iRBC adheres to the wall for a longer time frame, which in turn hinders the motion of the cell through the narrow capillary. The hRBC from its initial biconcave shape undergoes severe deformation to form an elongated elliptic shape, as it passes through the narrow channel of width $h = 4r_c$ (see Figure 15). The motion of iRBC passing through the tapered channel can also be noticed with a much longer passage time due to an initial jamming effect. Eventually, iRBC could also pass through the microfluidic channel, when there is higher flow rate. Figure 15 compares the transient deformation of hRBC as well as iRBC through the narrow microchannel. The constricted tapered region hinders the motion of the iRBC, thereby increasing the passage time. The time taken by the iRBC is almost twice as compared with that of hRBC in traversing through the capillary length of $20r_c$, which is attributed to severe deformation of the latter.

The transient evolution of deformation index (DI) as the RBC passes through the tapered channel of width $6r_c$ is presented in Figure 16. The DI is defined as $\mathrm{DI} = l/w$, where l and w are the lengths of RBC in the axial and transverse directions, respectively. The transient time for hRBC is about 100, while the corresponding passage time for iRBC is about 150 units for a flow rate of 1.5652. For a higher flow rate of 2.8057, the passage time was found to be 50 units for hRBC and 70 for the iRBC. Corresponding temporal variation of DI for hRBC and iRBC is presented in Figure 17. A steep rise in DI can be noticed for hRBC, as it passes through the constricted segment. On the contrary, cell deforms much more gradually for the iRBC, indicating a much lower rate of deformation. As the flow rate increases, the gradual deformation of iRBC is exemplified through an increased DI value of 1.3, as it passes through the tapered channel. The
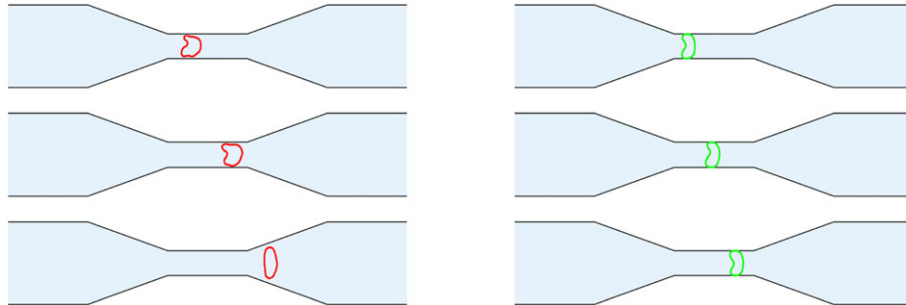

FIGURE 14 Deformation dynamics of a single red blood cell (RBC) in a tapered microchannel of width $h = 6r_c$ for flow rate $Q = 1.5652$. Left section shows the position of the healthy RBC (indicated by red color), whereas the right column shows the position of an infected RBC at the schizont state (indicated by green color)
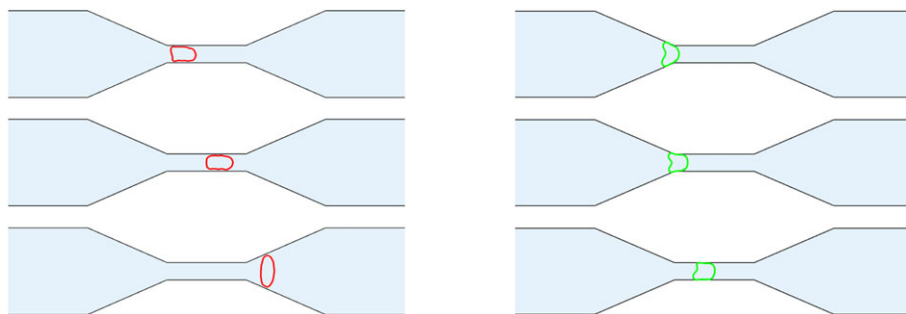

FIGURE 15 Deformation of a single red blood cell (RBC) in a tapered microchannel of width $h = 4r_c$ for flow rate $Q = 0.9828$. Left section shows the position of the healthy RBC (indicated by red color), whereas the right column shows the position of an infected RBC at the schizont state (indicated by green color)
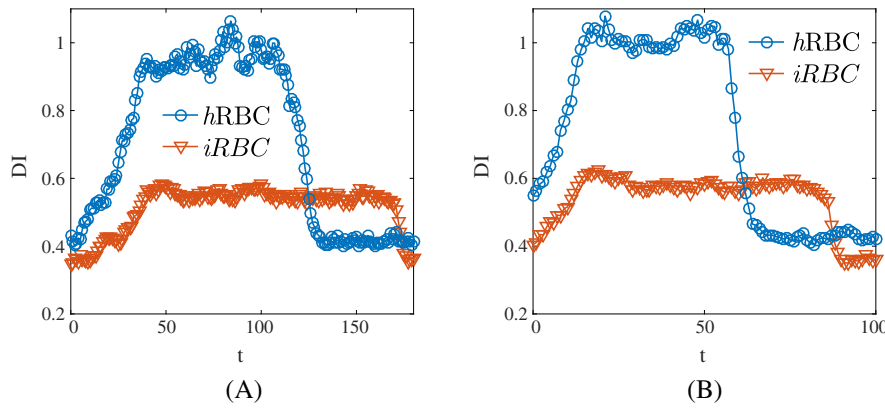
FIGURE 16 Deformation index (DI) of a healthy red blood cell (hRBC) and infected red blood cell (iRBC) in a tapered microchannel of width $6r_c$ for flow rates A, 1.5652 and B 2.8057, respectively
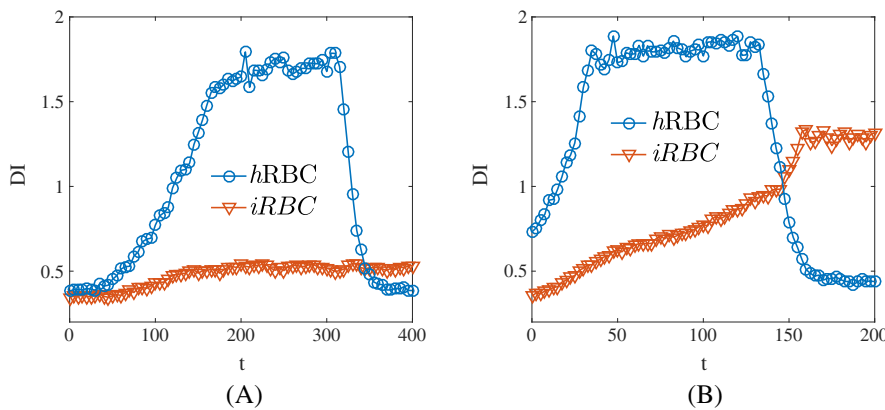

FIGURE 17 Deformation index (DI) of a healthy red blood cell (hRBC) and infected red blood cell (iRBC) in a tapered channel of width $4r_c$ for flow rates A, 0.568 and B, 0.9828, respectively

DI for hRBC is about 1.8, which is almost independent of flow rate. The effect of flow rate on RBC deformability is almost negligible for a $6r_c$ wide microchannel (see Figure 16). This is attributed to the comparable size of iRBC with that of microchannel. However, the flow rate effect is more prominent for flow through the micro capillary of $4r_c$ width. For a reduced flow rate, the iRBC completely blocks the microcapillary of width $4r_c$, while the hRBC could squeeze through the micro channel (see Figure 18). The deformation of iRBC is much less as it passes through the microcapillary at a lower flow rate of 0.568. A small layer between the wall and cell membrane is observed for hRBC, while the iRBC tries to adhere to the wall. The effect of flow rates on passage and blockage of RBCs is presented in Table 2. These results are qualitatively in good agreement with experimental results of Shelby et al[6] and particle-based simulations of Wu et al.[35]
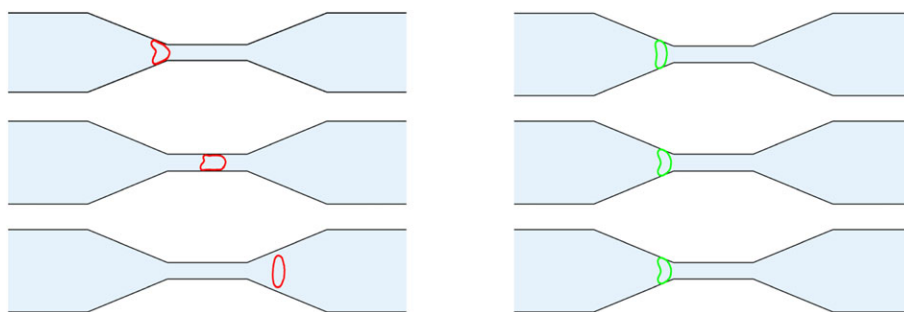

FIGURE 18 Deformation of a single red blood cell (RBC) in a converging-diverging tapered microfluidic channel of width $h = 4r_c$ for flow rate $Q = 0.568$. Left section shows the position of the healthy RBC (indicated by red color), whereas the right column shows the position of an infected RBC at the schizont state (indicated by green color)

TABLE 2   The effect of flow rate on passage and blockage of hRBC and iRBC through a tapered microchannel

	Width, h					
	$6r_c$			**$4r_c$**		
Flow rate, Q	2.8057	2.278	1.5652	0.9828	0.7987	0.568
hRBC	Passes	Passes	Passes	Passes	Passes	Passes
iRBC	Passes	Passes	Passes	Passes	Blocks	Blocks

Abbreviations: hRBC, healthy red blood cell; iRBC, infected red blood cell.

3.2.2 | The dynamics of RBC through a stenosed microchannel

The dynamics of a healthy and infected RBC through a semicircular constriction is termed as a stenosed microfluidic channel. This constriction is of particular interest, as it more closely resembles a stenosed artery, albeit without flexibility. The influence of flow rate and the degree of constriction on the passage characteristics are considered for both hRBC and iRBC. Simulations are performed for 40% and 80% degree of constriction. Figure 19 presents the motion of hRBC and iRBC in a 40% constricted microchannel. It can be seen that hRBC is severely deformed near the microvascular stenosed region compared with the iRBC. The iRBC could pass through the region as the width of the constriction is almost comparable with the size of the iRBC. For this 40% constriction, the transit time taken for both iRBC and hRBC is almost similar. However, this effect is more prominent when there is a severe constriction of 80% (see Figure 20). The hRBC could easily pass through the stenosed region due to its superior deformation characteristics. However, the iRBC was found to occlude the entry of this constriction, although it passes through for higher flow rates. Nevertheless, the transit time of iRBC was observed to be higher due to occlusion at the entry to the stenosed region of the microchannel.

Figure 21 shows the evolution of DI for hRBC and iRBC as the RBC passes through the stenosed microchannel with 40% constriction. The DI for healthy RBC is about 0.75, while it is 0.4 for iRBC for a flow rate of 3.6521. There is no significant difference in the transit time for the healthy and infected RBC. Also, the effect of flow rates on deformation of RBC is negligible. As the area of constriction is about 80%, a sharp increase in DI can be seen for hRBC as it flows
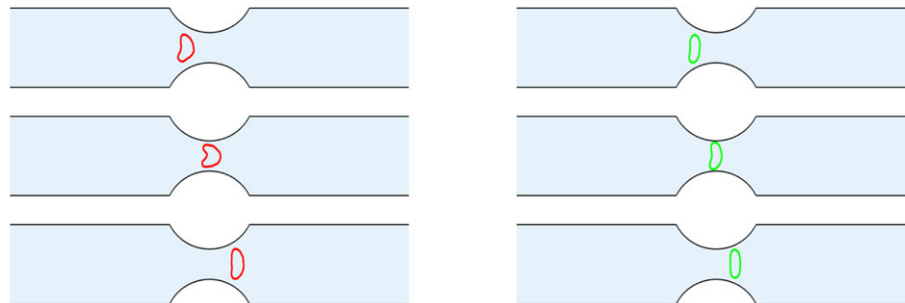
FIGURE 19   Deformation of a single red blood cell (RBC) in a stenosed microfluidic channel with 40% area constriction for flow rate, $Q = 3.6521$. Left section shows the position of the healthy RBC (indicated by red color), whereas the right column shows the position of an infected RBC at the schizont state (indicated by green color)

FIGURE 20   Deformation of a single red blood cell (RBC) in a stenosed microfluidic channel with 80% area constriction for flow rate $Q = 2.8745$. Left section shows the position of the healthy RBC (indicated by red color), whereas the right column shows the position of an infected RBC at the schizont state (indicated by green color)
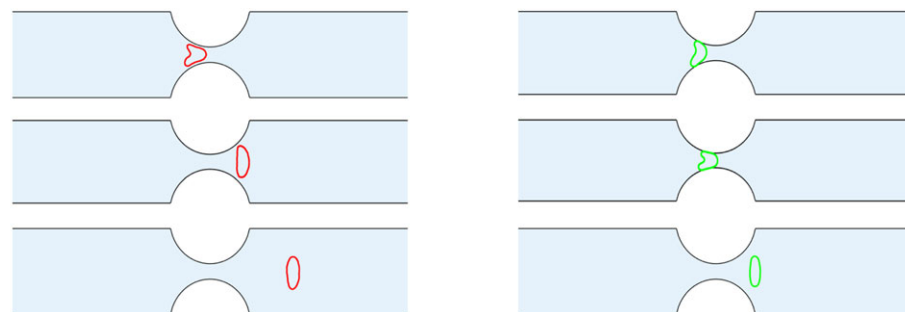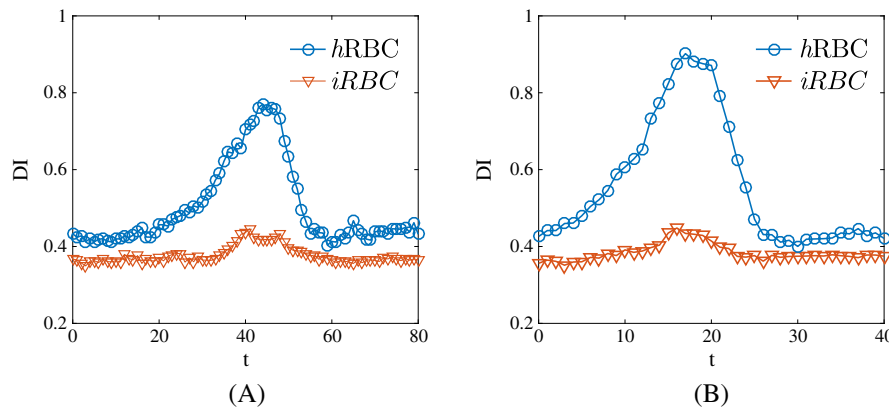
FIGURE 21 Deformation index (DI) of a healthy red blood cell (*h*RBC) and infected red blood cell (*i*RBC) in a stenosis-type microchannel with 40% area constriction for flow rates A, 3.6521 and B, 6.4892 respectively

through the stenosed type constriction. Figure 22 shows the transient evolution of DI of RBC passage through a stenosed microchannel. The *i*RBC deforms gradually to a DI of 0.6 and remain almost constant at flow rate of 1.7695. Thus, *i*RBC occludes the stenosed-type channel. As the flow rate is increased to 2.8745, the *i*RBC deforms gradually to pass through the constricted portion. The DI for *i*RBC is about 1.5 as it traverses past the constriction. The transient time for *h*RBC is only about 10, while the time taken by *i*RBC is about 40 units to traverse past the constriction.

The variation of flow rates and its effect on the passage of RBC are considered. For higher flow rate, the *h*RBC and *i*RBC squeeze past the stenosed microchannel. However, the transit time for *i*RBC is higher than that of *h*RBC, as the *i*RBC does not deform severely to pass through the stenosed section smoothly. Thus, the motion of *i*RBC is hindered because of the presence of constriction in the micro channel. As the flow rate decreases, the *i*RBC completely blocks the stenosed section as shown in Figure 23. The *h*RBC can still pass through the stenosed segment easily due to higher deformability. The effect of flow rate is summarized in Table 3.

As discussed earlier, the occlusion of *i*RBC depends on the stiffness of the cell membrane, the extent of constriction, and the viscous forces acting on the cell. The dynamics of RBCs in flow through the tapered microchannel of width $4r_c$
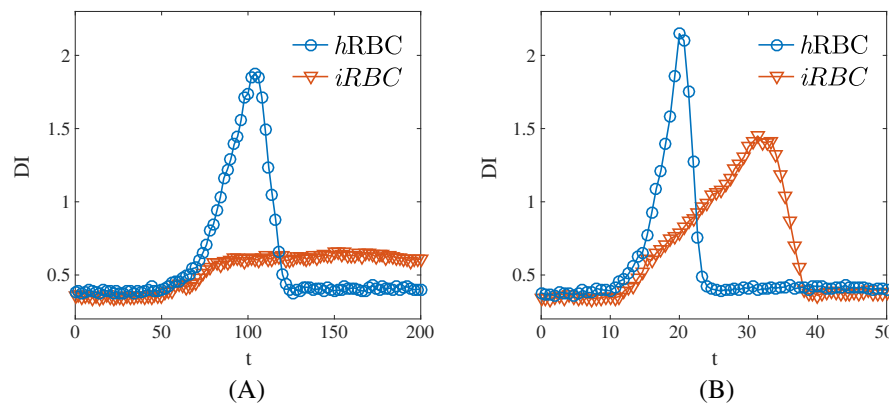

FIGURE 22 Deformation index (DI) of healthy red blood cell (*h*RBC) and infected red blood cell (*i*RBC) in a stenosis-type microchannel with 80% area constriction for flow rates A, 1.7695 and B, 2.8745 respectively
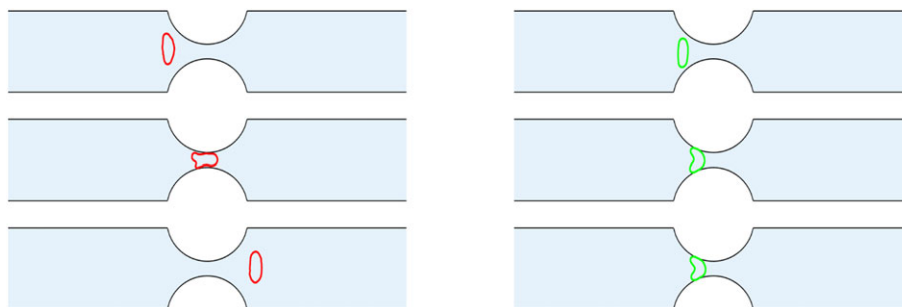

FIGURE 23 Deformation of a single red blood cell (RBC) in a stenosed microfluidic channel with 80% area constriction for flow rate $Q = 1.7695$. Left section shows the position of the healthy RBC (indicated by red color), whereas the right column shows the position of an infected RBC at the schizont state (indicated by green color)

TABLE 3 The effect of flow rate on passage and blockage of hRBC and iRBC through stenosed microchannel

	Degree of Constriction					
	40 %			80 %		
Flow rate, Q	6.4892	5.09	3.6521	2.8745	2.35	1.7695
hRBC	Passes	Passes	Passes	Passes	Passes	Passes
iRBC	Passes	Passes	Passes	Passes	Passes	Blocks

Abbreviations: hRBC, healthy red blood cell; iRBC, infected red blood cell.
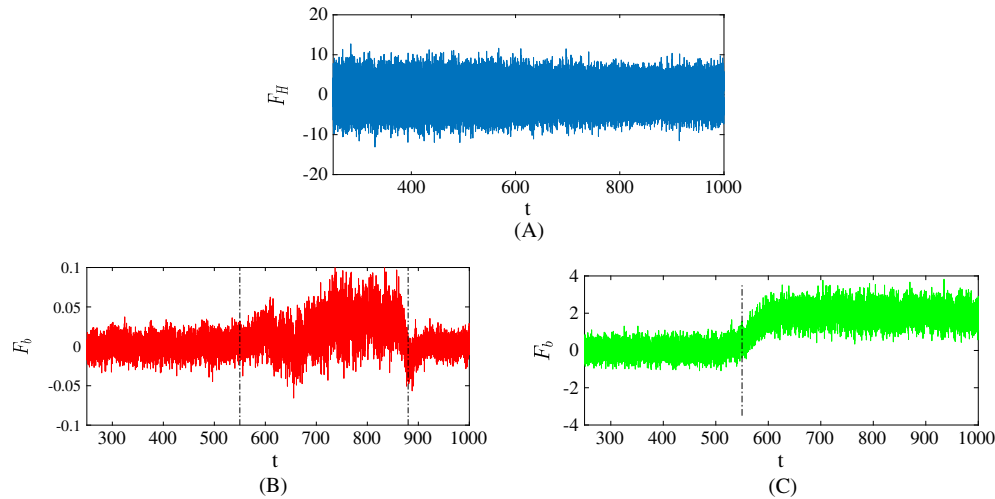
FIGURE 24 Comparison of bending forces with the hydrodynamics force corresponding to the flow rate of 0.568. A, Hydrodynamics force, bending force in streamwise direction for B, healthy red blood cell (RBC) and C, infected RBC

is considered for a detailed discussion on the role of the hydrodynamic forces on the passage-blockage characteristics of hRBC and iRBC. Figure 24 shows the hydrodynamic forces acting on the RBC and the corresponding bending forces of hRBC and iRBC in the streamwise direction. It is interesting to note that the bending forces of the hRBC is 1 order less than that of iRBC. As the hRBC squeezes through the constricted portion, the bending force marginally increases as shown in Figure 24B, which is very less compared with hydrodynamic forces that drives the cell. On the contrary, the value of bending force drastically increases and remains constant for the iRBC at the entrance of the constriction (shown as dashed line in Figure 24C). The hydrodynamics forces are not sufficient to overcome this bending force that results in occlusion. However, at higher flow rates, the hydrodynamic forces dominate over the bending force, which in turn helps the infected cell to pass through the constrictions. Similar trends were also observed in a stenosed-type microchannel.

4 | SUMMARY AND CONCLUSIONS

In the present study, the deformation dynamics of a healthy as well as an infected RBC through a microchannel is numerically simulated. A mesoscopic modeling approach, popularly known as FDPD, is used. A novel wall boundary modeling facilitated a reduction in the undesirable density fluctuations closer to the wall. Simulations are performed for flow through 2 types of microchannels, viz, (1) tapered microchannel and (b) stenosed microchannel. The discrete cell membrane was modeled using 50 FDPD particles connected by nonlinear WLC springs. The necessary bending rigidity for the RBC is obtained by choosing an appropriate bending potential for iRBC and hRBC. Similar to optical tweezers test of an experimental study, stretching of iRBC and hRBC was performed. Hence, the mechanical deformation characteristics of the hRBC as well as iRBC are obtained and validated against available experiments. The hRBC was found to undergo shape transition from an initial biconcave to a parachute-like shape under Poiseuille flow. The tank treading motion of hRBC membrane in shear flow was observed and quantified by finding the tank-treading frequency.

FDPD simulation of *h*RBC for flow through a tapered microchannel indicates its deformation into an elliptic shape. This simulation was found to be in good agreement with Quinn et al.[24] The motion of both healthy and infected cell in flow through a tapered channel indicates large deformation in the healthy RBC as opposed to much smaller deformation in the *i*RBC.

Corresponding deformability index was obtained for both healthy and infected RBCs. It was found that higher rigidity of *i*RBC makes it less deformable than that of *h*RBC. The *i*RBC was found to block the narrow capillary due to the rigidity of its cell membrane. Correspondingly, the passage time required was found to be much higher for the *i*RBC compared with *h*RBC. The flow rate was found to have a significant influence on the passage and blockage characteristics of RBCs, while passing through the constricted microfluidic channel. It was noticed that, as flow rate decreased below a certain critical value, the *i*RBC occludes at the inlet of the constriction and there by completely blocking the channel. It is hoped that an understanding of the *i*RBC occlusion phenomena may help in microfluidic device design for distinguishing the infected cells from the healthy one, reducing the need for multiple biochemical assaying.

ORCID

B. S. V. Patnaik iD http://orcid.org/0000-0002-4752-2602

REFERENCES

1. Nichols W, O'Rourke M, Vlachopoulos C. *Mcdonald's Blood Flow in Arteries. Theoretical, Experimental and Clinical Principles*. 6th Edn. London: Hodder Arnold; 2011.

2. Fung Y-C. *Biomechanics: Mechanical Properties of Living Tissues*. New York: Springer-Verlag; 1998.

3. Noguchi H, Gompper G. Shape transitions of fluid vesicles and red blood cells in capillary flows. *Proc Natl Acad Sci*. 2005;102:14159-14164.

4. Guo Q, Duffy S, Matthews K, et al.. Deformability based sorting of red blood cells improves diagnostic sensitivity for malaria caused by Plasmodium Falciparum. *Lab on a Chip*. 2016;16:645-654.

5. Faivre M, Abkarian M, Bickraj K, Stone H. Geometrical focusing of cells in a microfluidic device: an approach to separate blood plasma. *Biorheology*. 2006;43:147-59.

6. Shelby J, White J, Ganesan K, Rathod P, Chiu D. A microfluidic model for single-cell capillary obstruction by Plasmodium falciparum-infected erythrocytes. *Proc Natl Acad Sci*. 2003;100:14618-14622.

7. Guo Q, Reiling S, Rohrbach P, Ma H. Microfluidic biomechanical assay for red blood cells parasitized by Plasmodium Falciparum. *Lab on a chip*. 2012;12(6):1143-1150.

8. Guo Q, Park S, Ma H. Microfluidic micropipette aspiration for measuring the deformability of single cells. *Lab on a chip*. 2012;12(15):2687-95.

9. Freund J. Numerical simulation of flowing blood cells. *Annu Rev Fluid Mech*. 2014;46(1):67-95.

10. Ju M, Ye S, Namgung B, Cho S, Low H, Leo H, Kim S. A review of numerical methods for red blood cell flow simulation. *Comput Methods Biomech Biomed Engin*. 2015;18(2):130-140.

11. Ye T, Phan-Thien N, Lim C. Particle-based simulations of red blood cellsA review. *J Biomech*. 2016;49(11):2255-2266.

12. Mynard J, Nithiarasu P. A 1d arterial blood flow model incorporating ventricular pressure, aortic valve and regional coronary flow using the locally conservative Galerkin (LCG) method. *Commun Numer Methods Eng*. 2008;24(5):367-417.

13. Mynard J, Davidson M, Penny D, Smolich J. A simple, versatile valve model for use in lumped parameter and one-dimensional cardiovascular models. *Int J Numer Methods Biomed Eng*. 2012;28(6-7):626-641.

14. Melis A, Clayton R, Marzo A. Bayesian sensitivity analysis of a 1D vascular model with Gaussian process emulators. *Int J Numer Methods Biomed Eng*. 2017;33(12):1-11.

15. Ferranti F, Tamburrelli V, Antonini G. Rational macromodeling of 1d blood flow in the human cardiovascular system. *Int J Numer Methods Biomed Eng*. 2015;31(3):e02707.

16. Schiavazzi D, Baretta A, Pennati G, Hsia T, Marsden A. Patient-specific parameter estimation in single-ventricle lumped circulation models under uncertainty. *Int J Numer Methods Biomed Eng*. 2017;33(3):1-34.

17. Vahidkhah K, Balogh P, Bagchi P. Flow of red blood cells in stenosed microvessels. *Sci Rep*. 2016;6(June):28194.

18. Canuto D, Chong K, Bowles C, Dutson EP, Eldredge JD, Benharash P. A regulated multiscale closed-loop cardiovascular model, with applications to hemorrhage and hypertension. *Int J Numer Methods Biomed Eng*. 2018:1-25.

19. Pivkin IV, Karniadakis GE. Accurate coarse-grained modeling of red blood cells. *Phys Rev Lett*. 2008;101(11):1-4.

20. Fedosov DA, Noguchi H, Gompper G. Multiscale modeling of blood flow: from single cells to blood rheology. *Biomech Model Mechanobiol*. 2014;13(2):239-258.

21. Fedosov DA, Caswell B, Popel AS, Karniadakis GE. Blood flow and cell-free layer in microvessels. *Microcirculation*. 2010;17(8):615-628.

22. Fedosov DA, Caswell B, Karniadakis GE. A multiscale red blood cell model with accurate mechanics, rheology, and dynamics. *Biophys J*. 2010;98(10):2215-2225.

23. Pan W, Caswell B, Karniadakis GE. A low-dimensional model for the red blood cell. *Soft Matter*. 2010;6(18):4366.

24. Quinn DJ, Pivkin I, Wong SY, et al. Combined simulation and experimental study of large deformation of red blood cells in microfluidic systems. *Ann Biomed Eng*. 2011;39(3):1041-1050.

25. Bow H, Pivkin IV, Diez-Silva M, Goldfless SJ, et al. A microfabricated deformability-based flow cytometer with application to malaria. *Lab on a chip*. 2011;11(6):1065-73.

26. Salehyar S, Zhu Q. Deformation and internal stress in a red blood cell as it is driven through a slit by an incoming flow. *Soft matter*. 2016;12(13):3156-64.

27. Yazdani A, Deng M, Caswell B, Karniadakis GE. Flow in complex domains simulated by dissipative particle dynamics driven by geometry-specific body-forces. *J Comput Phys*. 2016;305:906-920.

28. Alizadehrad D, Fedosov DA. Static and dynamic properties of smoothed dissipative particle dynamics. *J Comput Phys*. 2018;356:303-318.

29. Gao C, Zhang P, Marom G, Deng Y, Bluestein D. Reducing the effects of compressibility in DPD-based blood flow simulations through severe stenotic microchannels. *J Comput Phys*. 2017;335:812-827.

30. Ranjith SK, Patnaik BSV, Vedantam S. No-slip boundary condition in finite-size dissipative particle dynamics. *J Comput Phys*. 2013;232(1):174-188.

31. Xiao LL, Chen S, Lin CS, Liu Y. Simulation of a single red blood cell flowing through a microvessel stenosis using dissipative particle dynamics. *MCB: Mol Cell Biomech*. 2014;11(1):067-085.

32. Hosseini SM, Feng JJ. How malaria parasites reduce the deformability of infected red blood cells. *Biophys J*. 2012;103(1):1-10.

33. Ye T, Phan-Thien N, Khoo BC, Lim CT. Stretching and relaxation of malaria-infected red blood cells. *Biophys J*. 2013;105(5):1103-1109.

34. Imai Y, Kondo H, Ishikawa T, Teck Lim C, Yamaguchi T. Modeling of hemodynamics arising from malaria infection. *J Biomech*. 2010;43(7):1386-1393.

35. Wu T, Feng JJ. Simulation of malaria-infected red blood cells in microfluidic channels: passage and blockage. *Biomicrofluidics*. 2013;7(4):044115-1–18.

36. Vahidkhah K, Fatouraee N. Numerical simulation of red blood cell behavior in a stenosed arteriole using the immersed boundary-lattice Boltzmann method. *Int J Numer Methods Biomed Eng*. 2012;28:239-256.

37. Nakamura BS, Wada MS. Analysis of red blood cell deformation under fast shear flow for better estimation of hemolysis. *Int J Numer Methods Biomed Eng*. 2013;30:42-54.

38. Pan TW, Wang T. Dynamical simulation of red blood cell rheology in microvessels. *Int J Numer Anal Model*. 2009;6(3):455-473.

39. Kaoui B, Krüger T, Harting J. How does confinement affect the dynamics of viscous vesicles and red blood cells? *Soft Matter*. 2012;8(35):9246.

40. Lázaro GR, Hernández-Machado A, Pagonabarraga I. Rheology of red blood cells under flow in highly confined microchannels: I. effect of elasticity. *Soft Matter*. 2014;10(37):7195.

41. Sinha K, Graham MD. Dynamics of a single red blood cell in simple shear flow. *Phys Rev E Stat Nonlinear Soft Matter Phys*. 2015;92(4):1-19.

42. Kaoui B, Harting J. Two-dimensional lattice Boltzmann simulations of vesicles with viscosity contrast. *Rheologica Acta*. 2016;55(6):465-475.

43. Niu X, Pan TW, Glowinski R. The dynamics of inextensible capsules in shear flow under the effect of the natural state. *Biomech Model Mechanobiol*. 2015;14(4):865-876.

44. Hariprasad DS, Secomb TW. Two-dimensional simulation of red blood cell motion near a wall under a lateral force. *Phys Rev E Stat Nonlinear Soft Matter Phys*. 2014;90(5):1-7.

45. Finken R, Kessler S, Seifert U. Micro-capsules in shear flow. *J Phys Condens Matter*. 2011;23(18):184113.

46. Sui Y, Chew YT, Roy P, Cheng YP, Low HT. Dynamic motion of red blood cells in simple shear flow. *Phys Fluids*. 2008;20:112106.

47. Skotheim JM, Secomb TW. Red blood cells and other nonspherical capsules in shear flow: oscillatory dynamics and the tanktreading-to-tumbling transition. *Phys Rev Lett*. 2007;98:078301.

48. Kaoui B, Biros G, Misbah C. Why do red blood cells have asymmetric shapes even in a symmetric flow?*Phys Rev Lett*. 2009;103(18):1-4.

49. Alizadeh A, Dadvand A. Effects of deformability of RBCs on their dynamics and blood flow passing through a stenosed microvessel: An immersed boundary-lattice Boltzmann approach. *Theor Comput Fluid Dyn*. 2018;32(1):91-107.

50. Müller K. In silico particle margination in blood flow. *Ph.D. Thesis*: Universität zu Köln; 2015.

51. Coupier G, Kaoui B, Podgorski T, Misbah C. Noninertial lateral migration of vesicles in bounded Poiseuille flow. *Phys Fluids*. 2008;20(11):111702.

52. Kaoui B, Ristow GH, Cantat I, Misbah C, Zimmermann W. Lateral migration of a two-dimensional vesicle in unbounded Poiseuille flow. *Phys Rev E Stat Nonlinear Soft Matter Phys*. 2008;77(2):1-9.

53. Müller K, Fedosov D, Gompper G. Margination of micro- and nano-particles in blood flow and its effect on drug delivery. *Sci Rep*. 2014;4:4871.

54. Dupire J, Abkarian M, Viallat A. A simple model to understand the effect of membrane shear elasticity and stress-free shape on the motion of red blood cells in shear flow. *Soft Matter*. 2015;11(42):8372-8382.

55. Hashemi Z, Rahnama M. Numerical simulation of transient dynamic behavior of healthy and hardened red blood cells in microcapillary flows. *Int J Numer Methods Biomed Eng*. 2016;e02763:1-12.

56. Shi L, Pan T-W, Glowinski R. Three-dimensional numerical simulation of red blood cell motion in Poiseuille flows. *Int J Numer Methods Biomed Eng*. 2014;76:397-415.

57. Nakamura M, Bessho S, Wada S. Spring network based model of a red blood cell for simulating mesoscopic blood flow. *Int J Numer Methods Biomed Eng*. 2013;29:114-128.

58. Fan X, Phan-Thien N, Chen S, Wu X, Ng TY. Simulating flow of DNA suspension using dissipative particle dynamics. *Phys Fluids*. 2006;18(6):063102-1–10.

59. Tsubota K-i, Wada S, Yamaguchi T. Simulation study on effects of hematocrit on blood flow properties using particle method. *J Biomed Sci Eng*. 2006;1(1):159-170.

60. Vijay Anand D, Patnaik BSV, Vedantam S. A dissipative particle dynamics study of a flexible filament in confined shear flow. *Soft Matter*. 2017;13(7):1472-1480.

61. Chapra SC, Canale R. *Numerical Methods for Engineers*. 5th ed. New York, NY, USA: McGraw-Hill, Inc.; 2006.

62. Groot RD, Warren PB. Dissipative particle dynamics: bridging the gap between atomistic and mesoscopic simulation. *J Chem Phys*. 1997;107(11):4423-4435.

63. Trofimov SY, Nies ELF, Michels MAJ. Thermodynamic consistency in dissipative particle dynamics simulations of strongly nonideal liquids and liquid mixtures. *J Chem Phys*. 2002;117(20):9383-9394.

64. Ranjith SK, Patnaik BSV, Vedantam S. Transport of DNA in hydrophobic microchannels: a dissipative particle dynamics simulation. *Soft matter*. 2014;10(23):4184-91.

65. Anand D. Vijay, Vedantam S, Patnaik B. S. V.. Dissipative particle dynamics simulation of shear flow in a microchannel with a deformable membrane. *Microfluid Nanofluid*. 2016;20(12):1-13.

66. Suresh S, Spatz J, Mills JP, et al.. Connections between single-cell biomechanics and human disease states: gastrointestinal cancer and malaria. *Acta Biomater*. 2005;1(1):15-30.

67. Tomaiuolo G, Simeone M, Martinelli V, Rotoli B, Guido S. Red blood cell deformation in microconfined flow. *Soft Matter*. 2009;5(19):3736.

68. Fedosov DA, Peltomäki M, Gompper G. Deformation and dynamics of red blood cells in flow through cylindrical microchannels. *Soft matter*. 2014;10(24):4258-67.

69. Fischer TM. Tank-tread frequency of the red cell membrane: dependence on the viscosity of the suspending medium. *Biophys J*. 2007;93(7):2553-2561.

70. Hosseini SM, Feng JJ. A particle-based model for the transport of erythrocytes in capillaries. *Chem Eng Sci*. 2009;64(22):4488-4497.

71. Cox RG, Zia IYZ, Mason SG. Particle motions in sheared suspensions XXV. Streamlines around cylinders and spheres. *J Colloid Interface Sci*. 1968;27(1):7-18.